Investigation of a Double-Negative Metamaterial-Loaded Helical Slow-Wave Structure: Equivalent Circuit Analysis Approach

Aditya Singh Thakur, *Graduate Student Member, IEEE*, Meenakshi Rawat, *Member, IEEE*, Manfred Thumm, *Life Fellow, IEEE*, and M. V. Kartikeyan, *Fellow, IEEE*

***Abstract*— This article presents a comprehensive theoretical investigation into a double-negative metamaterial (MTM)-loaded helical slow-wave structure (DNM-HSWS) employing an equivalent circuit analysis (ECA) approach considering the sheath-helix model of the helix. The study involves deriving dispersion and interaction impedance formulations, with a focus on analyzing the propagation and interaction characteristics of the structure. The practically feasible DNM-HSWS is designed and analyzed using CST-microwave studio software. A comparative analysis is conducted between theoretical and simulation results for the designed CST model, verifying the accuracy of the proposed theoretical investigation for the DNM-HSWS. Beyond validation, this study highlights the practical utility of the proposed theoretical investigations and the designed DNM-HSWS within the domain of MTM-inspired vacuum electron device (VED) applications. The findings contribute to advancing the understanding and application of MTM-loaded structures for improved performance in microwave devices.**

***Index Terms*— Backward-wave oscillators (BWOs), dispersion derivation, double-negative metamaterial (DNM), equivalent circuit analysis (ECA), slow-wave structure (SWS), vacuum electron device (VED).**

I. Introduction

THE evolution of vacuum electron devices (VEDs) is witnessed a transformative influence from metamaterial (MTM) inspired structures, marking a significant stride in design and application efficiency. L everaging unique electromagnetic (EM) wave propagation properties, MTMs have propelled the development of MTM-VEDs, significantly enhancing their efficiency and output power [1]. In particular, MTM-VEDs emerge as miniaturized, efficient, and resonant structures capable of generating substantial RF power, reaching magnitudes of hundreds of megawatts within mere seconds of saturation [2]. In VEDs, MTMs are used to design the slow-wave structures (SWSs) for applications, such as backward-wave oscillators (BWOs) [3], [4] and traveling wave tubes (TWTs) [5]. The leveraging negative permittivity and permeability, negative refractive index, and reversed Cherenkov radiation characteristics, MTM structures facilitate the antiparallel flow of phase velocity and group velocity [6], [7]. This, in turn, enables the design of highly efficient high-power MTM-BWOs by slowing down wave propagation within the interaction circuit and enhancing beam-wave interaction probability [4]. Tailoring MTM-loaded SWSs based on their propagation characteristics, results in the design of epsilon negative [8], mu negative [9], and double negative MTM (DNM)-loaded SWSs [10]. Furthermore, MTMs are also used to design the helical-SWSs (HSWSs) and improve their operationality [11], [12], [13]. Literature reports the design and utilization of both DNM and double positive MTM (DPM)-loaded helical structures, each serving unique purposes; DNM structures are used to miniaturize the dimensions compared with its conventional counterpart [14] and DPMs are used for size enlargement of HSWS [15]. Notably, an HSWS loaded with different MTMs can exhibit varying propagation bandwidths, operation frequencies, and interaction characteristics. The diverse features and utility benefits of MTMs redefine the landscape of MTM-loaded SWS design, assisting in multidimensional applicability to explore MTM-VEDs and advancing frontiers of microwave device technology.

The metallic MTM-loaded SWSs and HSWSs have demonstrated their efficacy in designing structures for high-power microwave (HPM) generation. HSWSs, documented in articles [11], [12], [13], [14], [15], have demonstrated their instrumental role in advancing VED applications. Notably, the dispersive DNM-loaded HSWS (DNM-HSWS), as reported by Sharma and Pathak [11], seamlessly integrates conventional HSWS characteristics with the unique properties of MTMs. It facilitates fundamental mode propagation with a significant reduction in wave propagation, featuring highly diminished group velocity and nearly constant phase velocity.

Aditya Singh Thakur and Meenakshi Rawat are with the Department of Electronics and Communication Engineering, Indian Institute of Technology Roorkee, Roorkee, Uttarakhand 247667, India.

Manfred Thumm is with the Institute for Pulsed Power and Microwave Technology (IHM), Karlsruhe Institute of Technology (KIT), 76131 Karlsruhe, Germany.

M. V. Kartikeyan is with the Department of Electronics and Communication Engineering, Indian Institute of Technology Roorkee, Roorkee 247667, India, and also with the Indian Institute of Information Technology, Design and Manufacturing (IIITDM), Kancheepuram, Chennai 600127, India (e-mail: kartik@ieee.org).

In addition, a DPM-loaded HSWS, detailed in article [15], strategically manipulates dispersion characteristics to achieve size enlargement for slow-wave devices at higher frequencies. This structure exhibits dispersion characteristics with notably higher interaction impedance across a broader bandwidth, rendering it suitable for high-power and high-efficiency wideband TWTs. Furthermore, a DNM-HSWS, as detailed in the article [14], serves the dual purpose of enabling both forward-wave (FW) and backward-wave (BW) propagation for TWTs and BWOs, respectively. The theoretical and simulation analyses conducted for this DNM-HSWS design showcased advanced slow-wave propagation and improved interaction characteristics compared with their conventional counterparts. These findings underscore the instrumental role of MTM assistance in HSWSs for enhancing the performance and capabilities of VEDs.

This article examines the propagation and interaction characteristics of a previously designed DNM-HSWS. A comprehensive theoretical analysis of the designed structure is conducted through an ECA approach, which is subsequently validated against previously reported EM field theory [14]. Furthermore, numerical outcomes from the ECA are compared with simulation results for the designed DNM-HSWS. The discrepancies between theoretical and simulation results are attributed to considerations of the sheath-helix model and the effective MTM medium employed in the theoretical analysis. This work is a follow-up of our previously published work [14], in which the theoretical analysis for a similar MTM model was carried out using the field analysis (FA) approach. The FA method involved a solution for a complex 6×6 matrix to derive the dispersion relationship. Whereas, the proposed ECA method provides a more straightforward and simplified approach by calculating only two key equivalent parameters: the inductance per unit length (L) and the capacitance per unit length (C). Moreover, this article extended beyond the basic derivation of the dispersion relation by performing a detailed parametric study to examine the impact of structural parameters on the EM characteristics. This comprehensive analysis is crucial for minimizing discrepancies between theoretical and simulation results while acknowledging the inherent limitations.

The structure of this article unfolds as follows. Section II presents the ECA approach for the DNM-HSWS, encompassing theoretical derivations for the dispersion relation and interaction impedance. Section III delves into numerical investigation, including a comparative study contrasting theoretically obtained results using the ECA approach with previously reported FA outcomes and simulation results for the designed DNM-HSWS. Finally, the conclusion drawn from the study is discussed in Section IV.

II. ECA of DNM-HSWS

Theoretical investigation into a DNM-HSWS is conducted utilizing an ECA approach [16], [17]. The design of the DNM structure, as depicted in Fig. 1(a), involves copper split-rings printed on a dielectric substrate of beryllia (BeO). Design parameters defining a single unit of the DNM structure are

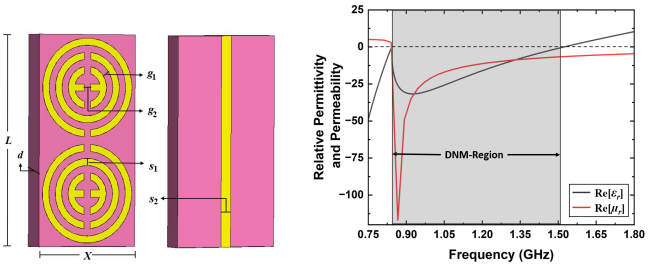

(a) (b)

Fig. 1. (a) Design of the DNM structure and (b) plot illustrating the relative permittivity and permeability as functions of frequency, defining the range of the DNM region from 0.85 to 1.50 GHz for the proposed DNM structure.

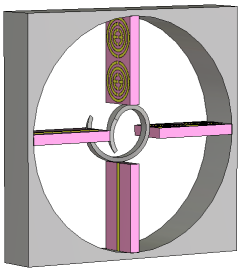

Fig. 2. Unit-cell structure design of the investigated DNM-HSWS.

TABLE I
DESIGN PARAMETERS (IN MILLIMETERS)

s_1	s_2	g_1	g_2	d	L	X	a	b	P
1	1.5	1	1.5	4	30	14	10	40	15

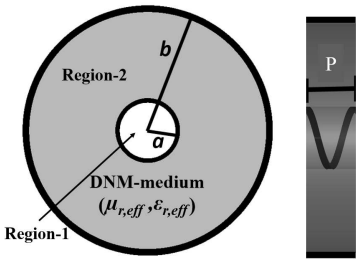

(a) (b)

Fig. 3. (a) Cross-sectional view and (b) side view depiction of the equivalent model of DNM-HSWS used for theoretical investigation.

outlined in Table I, where L, X, and d denote the length, width, and thickness of the structure, respectively. This configuration establishes a DNM regime within the frequency range of 0.85–1.50 GHz, characterized by negative values of relative permittivity (ε_r) and relative permeability (μ_r), simultaneously, as depicted in Fig. 1(b). Fig. 2 illustrated the design of the DNM-HSWS, where the helix of radius $a = 1$ cm and pitch angle $\phi = 13.5°$ loaded inside a cylindrical envelope of radius $b = 4$ cm and supported by DNM structures.

For the ECA of the proposed DNM-HSWS, Rowe's treatment for a sheath-helix model is adopted [18]. This treatment conceptualizes the helix as being enclosed within a cylindrical envelope and surrounded by an effective MTM medium between the helix and the cylindrical waveguide, as illustrated in Fig. 3. The effective relative permittivity $[\varepsilon_{r,\mathrm{eff}}(\omega)]$ and

permeability [$\mu_{r,\text{eff}}(\omega)$] in Region 2 of the theoretical model are determined using the relative permittivity (ε_r) and permeability (μ_r) values obtained from the simulation of the designed DNM structure (as illustrated in Fig. 1). The values of $\varepsilon_{r,\text{eff}}(\omega)$ and $\mu_{r,\text{eff}}(\omega)$ are calculated using the following relations [12]:

$$\varepsilon_{r,\text{eff}}(\omega) = 1 + (\varepsilon_r(\omega) - 1)\left[\frac{Nd}{\pi a(1+R)}\right] \tag{1}$$

$$\mu_{r,\text{eff}}(\omega) = 1 + (\mu_r(\omega) - 1)\left[\frac{Nd}{\pi a(1+R)}\right] \tag{2}$$

where N represents the number of MTM structure units arranged azimuthally in the DNM-HSWS (refer to Fig. 2), d denotes its thickness and R signifies the ratio of the waveguide radius b to the helix radius a. The effective range of DNM regime for the theoretical DNM-HSWS model is calculated using (1) and (2), ranging from 0.85 to 1.30 GHz.

A. EM Field Expressions

The field components corresponding to the propagating EM wave along the z-axis are computed for the DNM-HSWS model under consideration for ECA, as illustrated in Fig. 3. Utilizing Borgnis' potentials [11], the electric and magnetic field components, derived using [19], are as follows:

$$E_{z,i} = -{k_i}^2[A_i I_n(k_i\rho) + B_i K_n(k_i\rho)] \tag{3}$$

$$E_{\rho,i} = \Bigg[-(j\beta k_i)[A_i I_n'(k_i\rho) + B_i K_n'(k_i\rho)] + \frac{\omega\mu_i n}{\rho}[C_i I_n(k_i\rho) + D_i K_n(k_i\rho)]\Bigg] \tag{4}$$

$$E_{\theta,i} = \Bigg[\frac{n\beta}{\rho}[A_i I_n(k_i\rho) + B_i K_n(k_i\rho)] + (j\omega\mu_i k_i)\big[C_i I_n'(k_i\rho) + D_i K_n'(k_i\rho)\big]\Bigg] \tag{5}$$

$$H_{z,i} = -{k_i}^2\big[C_i I_n(k_i\rho) + D_i K_n(k_i\rho)\big] \tag{6}$$

$$H_{\rho,i} = \Bigg[-\frac{\omega\varepsilon_i n}{\rho}[A_i I_n(k_i\rho) + B_i K_n(k_i\rho)] - (j\beta k_i)\big[C_i I_n'(k_i\rho) + D_i K_n'(k_i\rho)\big]\Bigg] \tag{7}$$

and

$$H_{\theta,i} = \Bigg[-(j\omega\varepsilon k_i)[A_i I_n'(k_i\rho) + B_i K_n'(k_i\rho)] + \frac{n\beta}{\rho}[C_i I_n(k_i\rho) + D_i K_n(k_i\rho)]\Bigg]. \tag{8}$$

In the context of cylindrical coordinate system, ρ, θ, and z represent the transverse, azimuthal, and longitudinal components of the electric (E) and magnetic (H) fields, respectively. Moreover, in the above field expressions, the RF dependence of $e^{j(\omega t-\beta z)}$ is understood [16], [17], [20]. The designation i denotes the region through which the field propagates, where $i = 1$ corresponds to Region 1 ($0 < \rho < a$) and $i = 2$ corresponds to Region 2 ($a < \rho < b$). In Fig. 3(a), Region 1 represents the vacuum or air region, whereas Region 2 is the effective MTM region filled with $\varepsilon_{r,\text{eff}}(\omega)$ and $\mu_{r,\text{eff}}(\omega)$ medium. Depending upon the higher interaction and the dual-mode propagation characteristics of the designed DNM-HSWS, the order of Bessel's function is chosen as $n = 1$ [14]. Within this framework, $I_n(k_i\rho)$ and $K_n(k_i\rho)$ represent the modified Bessel functions of the first and second kinds, respectively, while $I_n'(k_i\rho)$ and $K_n'(k_i\rho)$ denote their respective first derivatives. Here, n signifies the order of modified Bessel functions. The radial propagation constant k_i can be defined in terms of the axial propagation constant β and the free space propagation constant k_0 through the following expression:

$$k_i = \sqrt{\beta^2 - \varepsilon_{r,i}\,\mu_{r,i}\,{k_0}^2}. \tag{9}$$

The undetermined field coefficients, denoted by A_i, B_i, C_i, and D_i, within the expressions representing the EM field components, are resolved by applying boundary conditions at the interfaces of the helix and cylindrical envelope. Subsequently, establishing the circuit equivalence for the theoretical model allows for the derivation of expressions governing the capacitance per unit length and the inductance per unit length. From these derived expressions, the dispersion relationship is established.

The theoretical model of the DNM-HSWS incorporates two boundaries: one at the helix and the other at the cylindrical envelope. Accordingly, the boundary conditions at the helix ($\rho = a$) and the cylindrical waveguide ($\rho = b$) can be expressed [19]. Utilizing the boundary conditions, the values of unknown field coefficients are determined and outlined as follows:

$$B_1 = D_1 = 0 \tag{10}$$

$$B_2 = \left[\frac{\cot\phi}{P_2} - \left(1 - \frac{P_1}{P_2}\cot\phi\right)\left(\frac{Q_2}{Q_1P_2 - Q_2P_1}\right)\right] \tag{11}$$

$$D_2 = \left[\left(1 - \frac{P_1}{P_2}\cot\phi\right)\left(\frac{P_2}{Q_1P_2 - Q_2P_1}\right)\right] \tag{12}$$

$$A_1 = -B_2\left[\frac{k_2}{k_1}\right]^2\frac{X}{I_n(k_1a)} \tag{13}$$

$$A_2 = -B_2\left[\frac{K_n(k_2b)}{I_n(k_2b)}\right] \tag{14}$$

$$C_1 = B_2\left[\frac{n\beta}{a}\frac{({k_2}^2 - {k_1}^2)}{\omega\mu_1{k_1}^3}\right]\frac{X}{I_n'(k_1a)} - D_2\left[\frac{\mu_2k_2}{\mu_1k_1}\frac{Z}{I_n'(k_1a)}\right] \tag{15}$$

$$C_2 = -D_2\left[\frac{K_n'(k_2b)}{I_n'(k_2b)}\right] \tag{16}$$

where

$$P_1 = \left(\frac{n\beta}{a}\right)^2\frac{{k_1}^2 - {k_2}^2}{\omega\mu_1{k_1}^3}\left[\frac{I_n(k_1a)}{I_n'(k_1a)}\right]ZX - (\omega\varepsilon_2k_2)ZY_1 + \omega\varepsilon_1\frac{{k_2}^2}{k_1}\left[\frac{I_n'(k_1a)}{I_n(k_1a)}\right]ZX \tag{17}$$

$$P_2 = \left(\frac{n\beta}{a}\right)\frac{{k_1}^2 - {k_2}^2}{\omega\mu_1k_1}\left[\frac{I_n(k_1a)}{I_n'(k_1a)}\right]ZX \tag{18}$$

$$Q_1 = \frac{n\beta}{a}\left(\frac{\mu_2k_2}{\mu_1k_1}\right)\left[\frac{I_n(k_1a)}{I_n'(k_1a)}\right]ZX - \frac{n\beta}{a}Y_2X \tag{19}$$

$$Q_2 = \left(\frac{\mu_2k_2k_1}{\mu_1}\right)\left[\frac{I_n(k_1a)}{I_n'(k_1a)}\right]ZX - ({k_2}^2)Y_2X \tag{20}$$

$$X = \left[\frac{I_n(k_2a)K_n(k_2b) - K_n(k_2a)I_n(k_2b)}{I_n(k_2b)}\right] \tag{21}$$

and

$$Z = \left[\frac{I_n'(k_2a)K_n'(k_2b) - K_n'(k_2a)I_n'(k_2b)}{I_n'(k_2b)}\right]. \quad (22)$$

B. Circuit Equivalence

The electric field of a propagating EM wave along axial direction can be defined in terms of scalar (Φ) and vector ($\vec{A}$) potentials, as follows:

$$E_{z,i} = -\frac{\partial \Phi}{\partial z} - \frac{\partial A_z}{\partial t}. \quad (23)$$

Since all the EM field components and potentials vary with the RF dependence of $e^{j(\omega t - \beta z)}$, (23) can be expressed as follows [20]:

$$E_{z,i} = j\beta\Phi - j\omega A_z \quad (24)$$

through

$$\frac{\partial}{\partial z} = -j\beta \;\; \& \;\; \frac{\partial}{\partial t} = j\omega. \quad (25)$$

These scalar (Φ) and vector (A_z) potentials for EM wave propagation obey the Lorentz condition

$$j\beta A_z - j\varepsilon_i\mu_i\omega\Phi = 0. \quad (26)$$

The components of the electric field, propagating in the axial direction of the structure, can be expressed in terms of scalar potential Φ in accordance with the above-mentioned (24) and (26) as follows:

$$E_{z,i} = \frac{{k_i}^2}{\omega\beta} j\omega\Phi = \frac{{k_i}^2}{\omega\beta}\frac{\partial\Phi}{\partial t}. \quad (27)$$

The field equations (3) and (27) are used to determine the following expression:

$$\frac{\partial I_z}{\partial z} + \frac{2\pi a}{j\omega}\left(\frac{{k_1}^2}{{k_2}^2}\right)[B_2X]^{-1}\frac{\partial\Phi}{\partial t} = 0 \quad (28)$$

which is identified as the telegraphist's equations [21]

$$\frac{\partial I_z}{\partial z} + C\frac{\partial\Phi}{\partial t} = 0. \quad (29)$$

The values of the capacitance per unit length of an equivalent transmission line C, is determined as follows:

$$C = \frac{2\pi a}{\omega}\left(\frac{{k_1}^2}{{k_2}^2}\right)[B_2X]^{-1}. \quad (30)$$

Applying the sheath-helix condition, defining conduction along the winding direction, the electric field components E_z and E_θ at $\rho = a$ can be represented as follows:

$$E_z^a = -E_\theta^a \cot\phi. \quad (31)$$

Equation (31), along with (5) and (26), collectively determined the expression

$$\frac{\partial\Phi}{\partial z} + \frac{\beta^2}{k_1^2}\left[\frac{n\beta}{a\omega}B_2X - \mu_2k_2D_2Z\right]\frac{\cot\phi}{2\pi a}\frac{\partial I_z}{\partial t} = 0. \quad (32)$$

Equation (32) is identified in the another form of telegraphist's equation [21]

$$\frac{\partial\Phi}{\partial z} + L\frac{\partial I_z}{\partial t} = 0 \quad (33)$$

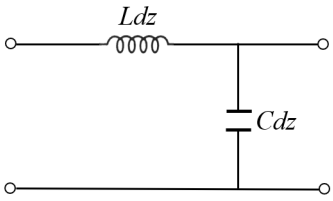

Fig. 4. Equivalent circuit model considered for the lossless DNM-HSWS. In this model, C and L denote the capacitance per unit length and the inductance per unit length of the structure, and dz is a length increment.

where L is the inductance per unit length for the equivalent transmission line and it is determined as follows:

$$L = \frac{\beta^2}{k_1^2}\left[\frac{n\beta}{a\omega}B_2X - \mu_2k_2D_2Z\right]\frac{\cot\phi}{2\pi a}. \quad (34)$$

Following the calculation of the capacitance per unit length and inductance per unit length for the proposed DNM-HSWS (as illustrated in Fig. 2), its equivalent circuit can be represented by a simple LC circuit as shown in Fig. 4. The capacitance per unit length for the equivalent circuit is defined by (30), while the inductance per unit length is defined by (34).

C. Expression for the Dispersion Relation

In the context of the analyzed theoretical model, the dispersion relation is expressed in terms of capacitance per unit length and inductance per unit length as $\beta^2 = \omega^2LC$. By substituting here the values of C and L obtained from (30) and (34), respectively, the final expression for the dispersion relationship for the DNM-HSWS is derived as follows:

$$XY_2 - \left[\frac{\mu_2k_2}{\mu_1k_1}\frac{I_n(k_1a)}{I_n'(k_1a)} + \frac{\omega^2\varepsilon_1\mu_2k_1k_2a^2}{(n\beta - {k_1}^2\tan\phi)^2}\frac{I_n'(k_1a)}{I_n(k_1a)}\right]XZ + \frac{\omega^2\varepsilon_2\mu_2{k_2}^2a^2}{(n\beta - {k_1}^2\tan\phi)^2}ZY_1 = 0 \quad (35)$$

where

$$Y_1 = \left[\frac{I_n'(k_2a)K_n(k_2b) - K_n'(k_2a)I_n(k_2b)}{I_n(k_2b)}\right] \quad (36)$$

$$Y_2 = \left[\frac{I_n(k_2a)K_n'(k_2b) - K_n(k_2a)I_n'(k_2b)}{I_n'(k_2b)}\right]. \quad (37)$$

If the structure is considered as lossless, then its characteristics impedance (Z_0) is defined as follows [22]:

$$Z_0 = \sqrt{\frac{L}{C}}. \quad (38)$$

By substituting the value of L and C from (34) and (30), respectively, the final expression for characteristics impedance is determined as follows:

$$Z_0 = \frac{B_2X\beta k_2}{2\pi a{k_1}^2}\sqrt{\omega\cot\phi\left[\frac{n\beta}{a} - {\mu_2k_2}^2\frac{D_2Z}{B_2X}\right]}. \quad (39)$$

D. Expression for the Interaction Impedance

The interaction impedance measures the magnitude of the axial electric field available for interaction with the electron beam inside the interaction structure. As defined by

Pierce [23], the interaction impedance of the structure is expressed as follows:

$$K = \frac{\|E_z\|^2}{2\beta^2 P_T} \tag{40}$$

where P_T is the total power propagating inside the interaction structure. The resulting expression for the total power is determined following [24] which is formulated as follows:

$$P_T = \pi\omega\beta[(\varepsilon_1 {A_1}^2 + \mu_1 {C_1}^2)I_1 + (\varepsilon_2 {A_2}^2 + \mu_2 {C_2}^2)I_2 + (\varepsilon_2 {B_2}^2 + \mu_2 {D_2}^2)I_3 + 2(\varepsilon_2 A_2 B_2 + \mu_2 C_2 D_2)I_4] \tag{41}$$

where

$$I_1 = \int_0^a \left[k_1{}^2[I_n'(k_1\rho)]^2 + n^2\frac{[I_n(k_1\rho)]^2}{\rho^2}\right]\rho d\rho \tag{42}$$

$$I_2 = \int_a^b \left[k_2{}^2[I_n'(k_2\rho)]^2 + n^2\frac{[I_n(k_2\rho)]^2}{\rho^2}\right]\rho d\rho \tag{43}$$

$$I_3 = \int_a^b \left[k_2{}^2[K_n'(k_2\rho)]^2 + n^2\frac{[K_n(k_2\rho)]^2}{\rho^2}\right]\rho d\rho \tag{44}$$

$$I_4 = \int_a^b \left[k_2{}^2[I_n'(k_2\rho)K_n'(k_2\rho)] + n^2\frac{[I_n(k_2\rho)K_n(k_2\rho)]}{\rho^2}\right]\rho d\rho. \tag{45}$$

Substitution of P_T from (41) into (40), results in the final expression for interaction impedance as follows:

$$K = \left[\frac{k_1{}^4}{2\pi\omega\beta^3}\right]F^{-1} \tag{46}$$

where

$$F = F_1 + F_2 + F_3 + F_4 \tag{47}$$

and

$$F_1 = \left[\varepsilon_1 + \mu_1\frac{C_1{}^2}{A_1{}^2}\right]\frac{I_1}{I_n^2(k_1\rho)} \tag{48}$$

$$F_2 = \left[\varepsilon_2\frac{A_2{}^2}{A_1{}^2} + \mu_2\frac{C_2{}^2}{A_1{}^2}\right]\frac{I_2}{I_n^2(k_1\rho)} \tag{49}$$

$$F_3 = \left[\varepsilon_2\frac{B_2{}^2}{A_1{}^2} + \mu_2\frac{D_2{}^2}{A_1{}^2}\right]\frac{I_3}{I_n^2(k_1\rho)} \tag{50}$$

$$F_4 = \left[\varepsilon_2\frac{A_2B_2}{A_1{}^2} + \mu_2\frac{C_2D_2}{A_1{}^2}\right]\frac{I_4}{I_n^2(k_1\rho)}. \tag{51}$$

III. Results and Discussion

In order to analyze the propagation and interaction characteristics of the proposed DNM-HSWS, the equations for dispersion relation (35) and the interaction impedance (46), derived through the ECA, are numerically investigated and plotted to determine the phase velocity and interaction impedance as a function of frequency. The commercial software MATLAB is used to develop the in-house codes and the Newton-Raphson method [25] is employed to obtain the roots of (35). The characteristic impedance, interaction impedance, and normalized phase velocity for the equivalent theoretical model are depicted in Fig. 5. In Fig. 5, the phase velocity is defined as $v_p = \omega/\beta$. The plots clearly indicate that the structure is an SWS, supporting both FW and BW propagations for the dominant mode. It exhibits

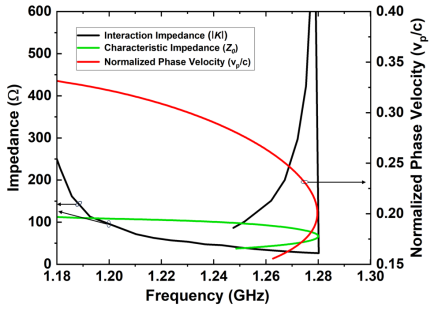

Fig. 5. Interaction impedance, characteristic impedance, and normalized phase velocity are plotted as a function of frequency for the theoretically analyzed equivalent circuit model. Here, *c* represents the speed of light in a vacuum.

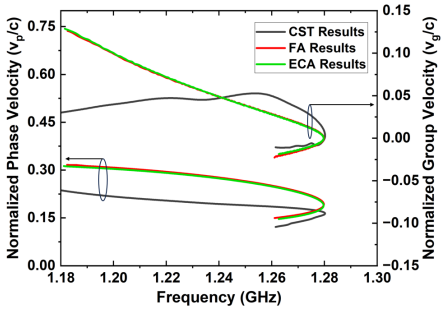

Fig. 6. Normalized phase and group velocities are plotted against frequency. The CST simulation results for designed DNM-HSWS (see Fig. 2) are plotted in black and theoretical outcomes using FA and ECA are plotted in red and green, respectively.

higher interaction near both the lower and higher frequency regions of the propagation band. At the lower frequencies, the dominant mode of propagation is the FW mode, whereas at the higher frequencies, the BW mode is the dominant mode of propagation. The numerically investigated results for derived dispersion relation (35) and interaction impedance (46) are compared with the results obtained using the EM FA approach, reported in [14]. Moreover, the numerical results are validated against simulation outcomes for the designed DNM-HSWS using CST-microwave studio.

Fig. 6 illustrates the propagation characteristics of the proposed DNM-HSWS. The plot depicted the normalized phase and group velocities against frequency, showcasing both BW and FW modes converging at the point of mode degeneracy for the dominant mode traveling through the DNM-HSWS. Notably, the propagation bandwidth of the structure appears narrow, spanning approximately from 1.18 to 1.28 GHz. The incorporation of the DNM structure within the HSWS enables BW propagation, suggesting potential applications in the design of highly resonant MTM-BWOs. The phase velocity plot illustrates the characteristic behavior of the proposed structure as an SWS, with the BW mode exhibiting slower propagation compared with the FW mode. Conversely, the group velocity plots in Fig. 6 illustrates that the BW mode propagates with a negative group velocity, signifying an antiparallel flow of phase and group velocities. This observation suggests that the BW mode experiences an extremely slow energy propagation, moving opposite to the direction of wave propagation. It increases the duration of beam-wave interaction

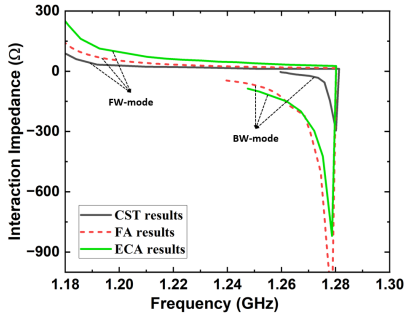

Fig. 7. Interaction impedances are plotted against frequency. The CST simulation results for designed DNM-HSWS (see Fig. 2) are plotted in black and theoretical outcomes using FA and ECA are plotted in red and green, respectively.

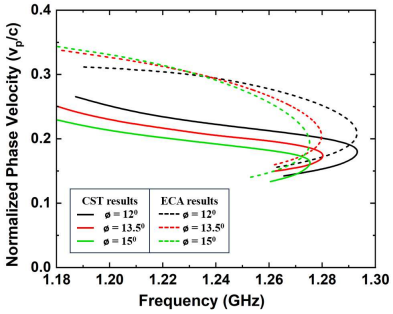

Fig. 8. Normalized phase velocity plotted against frequency, illustrating the impact of helix pitch angle (ϕ) variation on propagation characteristics and the discrepancy between theoretical (dashed lines) and simulation (solid lines) outcomes of the DNM-HSWS.

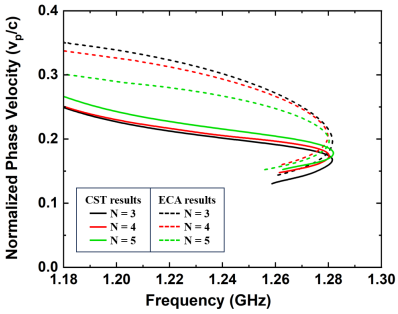

Fig. 9. Normalized phase velocity plotted against frequency, illustrating the impact of varying N (the number of DNM structures loaded between the helix and cylindrical waveguide) on propagation characteristics and the discrepancy between theoretical (dashed lines) and simulation (solid lines) outcomes of the DNM-HSWS.

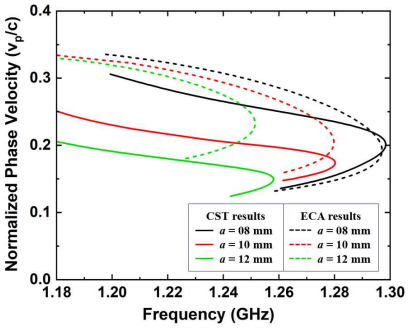

Fig. 10. Normalized phase velocity plotted against frequency, illustrating the impact of helix radius variation on propagation characteristics and the discrepancy between theoretical (dashed lines) and simulation (solid lines) outcomes of the DNM-HSWS.

within the structure, potentially facilitating the generation of high-efficiency RF signals. Furthermore, the degeneracy point represents the point where the mode of wave propagation becomes undefined and the energy flow approaches 0.

The interaction impedance, depicted as a function of frequency in Fig. 7, provides insight into the interaction characteristics of the examined DNM-HSWS for the FW mode and BW mode. The analysis reveals that interaction within the FW mode predominates in the lower frequency range of the propagation band. Conversely, the BW mode dominates the interaction in the higher frequency range, particularly in proximity to the mode-degeneracy point. This observation highlights the distinct interaction behaviors associated with FW and BW modes within the analyzed DNM-HSWS.

Figs. 6 and 7 collectively demonstrate a consistent correlation between the plots derived from ECA results and those obtained from the FA, thereby validating the theoretical investigation into the propagation and interaction characteristics using the ECA approach. Furthermore, the outcomes of simulation analysis of designed DNM-HSWS (as shown in Fig. 2) exhibit similarities to the theoretical plots, depicting both BW and FW modes, as well as the mode degeneracy. However, significant discrepancies exist between the theoretical and simulation results. These discrepancies can be attributed to several factors, including the considerations of effective DNM between the helix and cylindrical envelope, which is obtained using (1) and (2), and the sheath-helix having conductivity along the direction of helix winding with an infinitesimally small helix thickness. The differing trends in group velocities between the ECA and simulation analysis results (in lower frequency regions) are a direct consequence of the variations of propagation constant with frequency, emphasizing the importance of minimizing discrepancies between the dispersion plots obtained through ECA and CST simulations.

The influence of structural parameters on the EM properties of the designed DNM-HSWS is investigated through simulation results and shown in Figs. 8–10. This analysis involves the variation of the helix pitch angle (ϕ), helix radius (a), and the number of DNM structures (N) positioned between the helix and the cylindrical envelope. The following are inferred from these investigations.

1) Increasing the pitch angle causes the propagation band to shift toward lower frequencies and reduces phase velocity.
2) Change in a number of DNM structures inside the HSWS does not significantly affect the propagation band of the structure but the phase velocity increases for the larger number of DNM structures inside the unit cell.
3) Propagation band shifts toward lower frequencies and the phase velocity decreases for higher values of a, resulting in a higher interaction time for a larger helix radius.
4) From Fig. 8, it is evident that reducing ϕ minimized the discrepancy between simulation and theoretical results. Since the helix is assumed to be closely wound in the sheath-helix model, the theoretical results obtained through ECA for the sheath-helix model are more accurate and align better with simulation results at lower values of ϕ.

5) Furthermore, the discrepancy can also be minimized by increasing N and decreasing a (adhering to the condition $Nd < 2\pi a$), as shown in Figs. 9 and 10, respectively. Since the equivalent structure model incorporates parameters $\varepsilon_{r,\text{eff}}$ and $\mu_{r,\text{eff}}$ in the ECA frame work, by increasing N and decreasing a, the difference between the effective medium parameters of the theoretical model and the medium parameters of the DNM structure will get reduced. This leads to a decreased discrepancy between theoretical calculations and simulation results.

The discrepancy between simulation and theoretical results can further be reduced by considering the full-wave analysis with a practical helix with an actual medium surrounding it. These refinements in theoretical modeling ensure a more comprehensive understanding of the behavior of DNM-HSWS, facilitating improved accuracy in predicting its propagation and interaction characteristics and rendering the potential for the future scope of this work.

IV. Conclusion

The investigation conducted on the DNM-HSWS has been aimed at exploring its potential for MTM-inspired microwave device applications. Utilizing an ECA approach, the theoretical investigation has been provided foundational insights into the behavior of DNM-HSWS. The comparative analysis of results obtained from ECA and FA validates the efficacy of the ECA approach. The proposed DNM-HSWS emerged as a narrow band, miniaturized SWS, exhibiting very slow EM wave propagation near mode-degeneracy. Notably, the structure has supported BW propagation, characterized by the antiparallel flow of phase and group velocities due to the incorporation of the DNM structure, thus rendering it suitable for MTM-BWO applications. The observed discrepancy between theoretical and simulation results has been addressed by considering an equivalent theoretical model used in ECA investigations. To minimize the discrepancy, the variation of the helix pitch angle, helix radius, and the number of DNM structures loaded between the helix and cylindrical waveguide has been discussed. Overall, the study underscores the effectiveness of the investigated DNM-HSWS for SWS device applications, particularly in generating high-efficiency, highly resonant microwave signals, with promising prospects for designing VEDs.

References

[1] Z. Duan et al., "Metamaterial-inspired vacuum electron devices and accelerators," *IEEE Trans. Electron Devices*, vol. 66, no. 1, pp. 207–218, Jan. 2019, doi: 10.1109/TED.2018.2878242.

[2] J. W. Luginsland, J. A. Marshall, A. Nachman, and E. Schamiloglu, *High Power Microwave Sources and Technologies Using Metamaterials*. Hoboken, NJ, USA: Wiley, 2021.

[3] A. Singh Thakur, M. Rawat, and M. V. Kartikeyan, "Design of an oppositely-oriented circular split-ring resonator-loaded multibeam all-metallic metamaterial backward-wave oscillator," *IEEE Trans. Plasma Sci.*, vol. 51, no. 9, pp. 2625–2631, Sep. 2023, doi: 10.1109/TPS.2023.3305563.

[4] J. S. Hummelt, S. M. Lewis, M. A. Shapiro, and R. J. Temkin, "Design of a metamaterial-based backward-wave oscillator," *IEEE Trans. Plasma Sci.*, vol. 42, no. 4, pp. 930–936, Apr. 2014, doi: 10.1109/TPS.2014.2309597.

[5] Y. S. Tan and R. Seviour, "Wave energy amplification in a metamaterial-based traveling-wave structure," *EPL*, vol. 87, no. 3, p. 34005, Aug. 2009, doi: 10.1209/0295-5075/87/34005.

[6] V. G. Veselago, "The electrodynamics of substances with simultaneously negative values of ε and μ," *Sov. Phys. Uspekhi*, vol. 10, no. 4, pp. 509–514, Apr. 1968, doi: 10.1070/pu1968v010n04abeh003699.

[7] R. Marques, F. Martin, and M. Sorolla, *Metamaterials With Negative Parameters: Theory, Design, and Microwave Applications*. Chichester, U.K.: Wiley-Blackwell, 2007.

[8] S. C. Yurt, M. I. Fuks, S. Prasad, and E. Schamiloglu, "Design of a metamaterial slow wave structure for an O-type high power microwave generator," *Phys. Plasmas*, vol. 23, no. 12, Dec. 2016, Art. no. 123115, doi: 10.1063/1.4972535.

[9] H. Seidfaraji, A. Elfrgani, C. Christodoulou, and E. Schamiloglu, "A multibeam metamaterial backward wave oscillator," *Phys. Plasmas*, vol. 26, no. 7, Jul. 2019, Art. no. 073105, doi: 10.1063/1.5100159.

[10] Y. Wang et al., "S-band high-efficiency metamaterial microwave sources," *IEEE Trans. Electron Devices*, vol. 63, no. 9, pp. 3747–3752, Sep. 2016, doi: 10.1109/TED.2016.2593701.

[11] D. K. Sharma and S. K. Pathak, "Slowing and stopping of wave in dispersive metamaterial loaded helical guide," *Opt. Exp.*, vol. 24, no. 3, pp. 2687–2700, 2016, doi: 10.1364/oe.24.002687.

[12] N. Purushothaman and S. K. Ghosh, "Performance improvement of helix TWT using metamaterial helix-support structure," *J. Electromagn. Waves Appl.*, vol. 27, no. 7, pp. 890–900, May 2013, doi: 10.1080/09205071.2013.792748.

[13] A. K. Varshney, R. Guha, S. Biswas, P. P. Sarkar, S. K. Datta, and B. N. Basu, "Tape-helix model of analysis for the dispersion and interaction impedance characteristics of a helix loaded with a double-negative metamaterial for potential application in vacuum electron devices," *J. Electromagn. Waves Appl.*, vol. 33, no. 2, pp. 138–150, Jan. 2019, doi: 10.1080/09205071.2018.1530614.

[14] A. S. Thakur, M. Rawat, and M. V. Kartikeyan, "Analysis of a new metamaterial-loaded helical slow-wave structure for vacuum electron device applications," *IEEE Trans. Plasma Sci.*, vol. 52, no. 3, pp. 682–689, Mar. 2024, doi: 10.1109/TPS.2024.3373492.

[15] R. Guha and S. K. Ghosh, "Dispersion control and size enlargement of helical slow-wave structure by double-positive metamaterial assistance," *IEEE Trans. Electron Devices*, vol. 69, no. 2, pp. 771–776, Feb. 2022, doi: 10.1109/TED.2021.3134925.

[16] M. V. Kartikeyan, A. K. Sinha, H. N. Bandopadhyay, and D. S. Venkateswarlu, "A study of radially thick helix: Equivalent circuit approach," *IEEE Trans. Electron Devices*, vol. 39, no. 8, pp. 1961–1965, Aug. 1992, doi: 10.1109/16.144690.

[17] M. V. Kartikeyan, A. K. Sinha, H. N. Bandopadhyay, and D. S. Venkateswarlu, "Effective simulation of the radial thickness of helix for broad band, practical TWT's," *IEEE Trans. Plasma Sci.*, vol. 27, no. 4, pp. 1115–1123, Aug. 1999, doi: 10.1109/27.782291.

[18] J. E. Rowe, *Nonlinear Electron-Wave Interaction Phenomena*. New York, NY, USA: Academic, 1965.

[19] N. R. Vanderplaats, M. A. Kodis, and H. P. Freund, "Design of traveling wave tubes based on field theory," *IEEE Trans. Electron Devices*, vol. 41, no. 7, pp. 1288–1296, Jul. 1994, doi: 10.1109/16.293360.

[20] B. N. Basu, *Electromagnetic Theory and Applications in Beam-Wave Electronics*. Singapore: World Scientific, 1996.

[21] L. Weiss and W. Mathis, "Generalized telegraphist's equations for deformed waveguides," *Electromagnetics*, vol. 18, no. 4, pp. 353–365, 1998, doi: 10.1080/02726349808908594.

[22] D. M. Pozar, *Microwave Engineering: Theory and Techniques*. Hoboken, NJ, USA: Wiley, 2021.

[23] J. R. Pierce, *Travelling-Wave Tubes*. New York, NY, USA: D. Van Nostrand, 1950.

[24] B. J. Mcmurtry, "Fundamental interaction impedance of a helix surrounded by a dielectric and a metal shield," *IRE Trans. Electron Devices*, vol. 9, no. 2, pp. 210–216, Mar. 1962, doi: 10.1109/T-ED.1962.14972.

[25] S. C. Chapra and R. P. Canale, *Numerical Methods for Engineers*, 6th ed., Maidenhead, U.K.: McGraw-Hill, 2010.